Arabian Journal of Chemistry (2018) **11**, 1117–1125

King Saud University

Arabian Journal of Chemistry

www.ksu.edu.sa
www.sciencedirect.com

ORIGINAL ARTICLE

Water treatment by photodegradation on orthorhombic antimony sulfide powder and effect of key operational parameters using methyl orange as a model pollutant

Muhammad Muneeb [a], Bushra Ismail [b,*], Tanzeela Fazal [b], Rafaqat Ali Khan [b], Asad Muhammad Khan [b], Muhammad Bilal [c], Bakhtiar Muhammad [a], Abdur Rehman Khan [b]

[a] *Department of Chemistry, Hazara University Mansehra, Pakistan*
[b] *Department of Chemistry, COMSATS Institute of Information Technology, Abbottabad 22060, Pakistan*
[c] *Department of Environmental Chemistry, COMSATS Institute of Information Technology, Abbottabad 22060, Pakistan*

Received 20 October 2014; accepted 16 May 2015
Available online 23 May 2015

KEYWORDS

Chalcogenides;
Chemical preparation;
X-ray diffraction;
Photocatalysis

Abstract Photocatalytic treatment of colored wastewaters containing methyl orange was achieved using visible light active Sb_2S_3 photocatalyst powder. Antimony chloride and sodium sulfide were used as antimony and sulfur precursors, respectively, for the synthesis of Sb_2S_3 powder by the hydrothermal method. The temperature of the Teflon lined autoclave was maintained at 105, 150 and 200 °C for varying times of 4, 6 and 12 h and corresponding phase evolution was studied by X-ray diffraction. XRD showed well crystalline single phase orthorhombic Sb_2S_3 powder synthesized at the different temperatures of autoclave maintained for different times. From the view point of time and temperature efficiency, Sb_2S_3 powder synthesized at 105 °C/4 h was selected for further characterization and photocatalytic studies. Well grown spherical particles were observed under scanning electron microscope. Material was found to be thermally stable in temperature range of 25–1000 °C. Vibrational modes of metal-sulfur bonds were observed at wave numbers below 1000 cm^{-1} in the Fourier transform infrared spectrum at room temperature. BET surface area of the material was 65 m^2/g as obtained through N_2 adsorption experiments. The well characterized material was used for the degradation studies of methyl orange and the effect of various factors

---

[*] Corresponding author. Tel.: +92 992 383 591; fax: +92 992 383 441.
E-mail address: bushraismail@ciit.net.pk (B. Ismail).
Peer review under responsibility of King Saud University.

Production and hosting by Elsevier

http://dx.doi.org/10.1016/j.arabjc.2015.05.010

such as, pH, concentration of the solution, time, temperature and quantity of catalyst was investigated. Lower MO concentrations were degraded better and lower pH favored the degradation. The catalyst dosage had direct relationship with the degradation rate up to a certain limit. Pseudo first rate constant of 0.0012 min^{-1} was calculated from the fitting of kinetic data. Degradation rate increased with the increase in reaction temperature. Degradation mechanism was designed based on the characterization and photocatalytic studies.

1. Introduction

Water pollution is a key environmental issue as almost 4000 children die daily due to water born diseases (Malato et al., 2009) demanding extensive research efforts in the field of water treatment. Colored waters from paper, plastic, leather, food and textile industries (Vidhu and Philip, 2014) containing many toxic and nonbiodegradable organic compounds are disposed into water streams daily. For example, methyl orange is an azo dye used in the textile industries. It is mutagenic and when present in excess amounts, causes poor light penetration and hence, imbalance in aquatic ecosystems (Vidhu and Philip, 2014).

The conventional water treatment methods include coagulation, sedimentation, adsorption and activated sludge methods, to mention the few. However, recently the advanced oxidation processes that involve reactive $^{\bullet}OH$ radicals have gained much attention for the water treatment. Some peculiar properties of AOPs include, the nonselective nature (Dantas et al., 2003) and high oxidation potential (E^{o}) value of $\sim+2.80$ V vs NHE (Xu et al., 2013). These properties help in complete mineralization of the organic pollutants in water. The generation of $^{\bullet}OH$ radicals can be accomplished by UV assisted reaction systems containing H_2O_2/O_3 or by the use of semiconductor materials having wide band gaps (Dantas et al., 2003). Photons from sunlight having energies equal to or greater than the band gap energy of semiconductor are absorbed. The promotion of electrons from valence to conduction band results in the creation of holes in valence band. Secondary reactions of e and holes with oxygen and water respectively, result in the production of free radical species ($^{\bullet}OH$) and the degradation of the organic compound takes place over the surface of catalyst, the final products being CO_2 and H_2O (Litter, 1999; Casbeer et al., 2012; Di Paola et al., 2012) in case of complete mineralization of the pollutant.

The semiconductor material is preferred over a metallic one due to energy gap present in the semiconductor which reduces the chances of electron–hole recombination (Di Paola et al., 2012). TiO_2 is a UV active catalyst with a wide band gap of 3.2 eV (Najam Khan et al., 2014). TiO_2 has been used as a powder (Khataee et al., 2013), suspension (Morozova et al., 2011), membrane (Xiao et al., 2010) or thin film (Li, 2011). Research activities are underway to search for efficient and low cost photocatalyst materials having band gap values which correspond to wavelengths of visible light so that the utilization of 44% of visible light can be achieved as opposed to 4% UV light. Many visible light photocatalysts in the form of oxides (Nogueira et al., 2014) or sulfides (Saranya et al., 2014) having different morphologies, for example, nanowalls (Liu et al., 2014), nanorods (Korake et al., 2014), nanofibres (Lee et al., 2013), nanobelts (Liang et al., 2013) have been used so far. Visible light photocatalysts of the sulfide family are gaining much attention these days. Many reports on utilization of sulfide photocatalysts are found which include photocatalysis on CoS (Sohrabnezhad et al., 2009), CdS (Repo et al., 2013), CdS–ZnS (Antoniadou et al., 2011) and Ni_3S_2 (Wang et al., 2013). One of the members of chalcogenide series, Sb_2S_3 has recently gained attention due to its suitable optoelectronic properties for solar cell applications in particular (Christians and Kamat, 2013). It has band gap in the range of 1.5–1.8 eV (Zhu et al., 2008) and very few reports on its utilization as visible light photocatalyst have been published so far. For example, Sb_2S_3 powder having a low surface area of 4.72 m^2/g synthesized by solid state reaction method is used

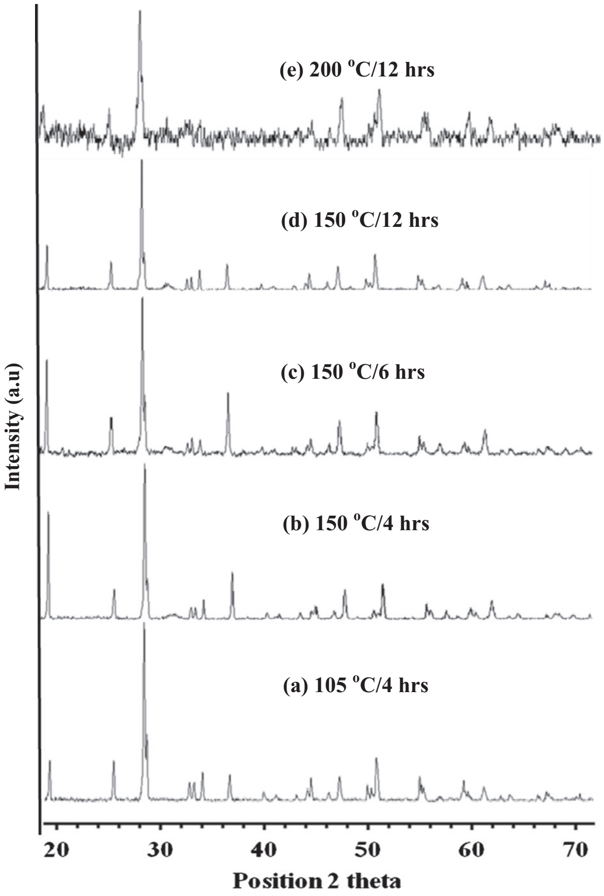

Figure 1 Comparison of the X-ray diffraction patterns of the Sb_2S_3 powders synthesized under variable conditions using hydrothermal method.

Table 1 Structural parameters of the synthesized samples calculated from the *d*-spacing values of the diffraction peaks.

Parameters	JCPDS: 03-065-2434	(a) 105 °C/4 h	(b) 150 °C/4 h	(c) 150 °C/6 h	(d) 150 °C/12 h	(e) 200 °C/12 h
a (Å)	11.302	12.60	12.4	11.36	11.36	12.50
b (Å)	11.222	10.80	10.8	11.22	11.26	10.58
c (Å)	3.834	3.80	3.97	3.95	3.93	4.4
V_{cell} (Å^3)	486	517	531	505	503	596
$\rho_{\text{X-ray}}$ (g/cm^3)	4.64	4.36	4.25	4.50	4.48	3.79
D (nm)	–	10	25	30	33	50

as visible light catalyst (Li et al., 2008). Nanorods and peanut shaped Sb_2S_3 with respective surface area of 5.57 and 3.06 m^2/g have also been used (Han et al., 2010). Similarly, TiO_2/Sb_2S_3 electrodes were used for the visible light driven photocatalysis (Bessegato et al., 2013). Nanorods of Sb_2S_3 having surface area of 15.1 m^2/g have been used as visible light photocatalysts (Sun et al., 2008). Chemical and biological inertness, cost, thermal stability and ease of availability are the key criteria for a good photocatalyst (Li and Zhang, 2012). The photocatalytic activity of a semiconductor depends upon particle size which in turn is related to the surface area of the material (Amano et al., 2013). Structure and property correlations are not given much emphasis and effect of key operational parameters such as pH, concentration, time and temperature has also not been given much attention. The design of mechanism of degradation requires a sound knowledge of the above mentioned parameters.

In the present study, we aim at the synthesis of high surface area Sb_2S_3 by hydrothermal method in the powder form for its use as photocatalysts. The effects of various factors such as, pH, concentration of the solution, catalysts dosage and temperature have been studied and correlated with characterization data in order to design a suitable mechanism for the degradation of methyl orange at the surface.

2. Experimental

2.1. Synthesis of Sb_2S_3

Analytical grade antimony chloride $SbCl_3$, urea $(NH_2)_2Co$, ethylene glycol $C_2H_6O_2$ and sodium sulfide Na_2S were purchased from Merck. In the hydrothermal method (Zhu et al., 2008) two separate solutions were prepared. 0.5 M solution of $SbCl_3$ was prepared by dissolving 0.346 g in 3 ml of ethylene glycol (EG) and 10 ml distilled water was added to this solution. 1.5 M Na_2S solution was prepared by dissolving 1.103 g in 10 ml distilled water. The two solutions were mixed together to get yellow suspension to which 30 ml of 1.5 M solution of urea was added. The mixtures were maintained individually at a temperature of 105, 150 and 200 °C for 4, 6 and 12 h in a Teflon lined autoclave. The resultant yellowish white suspension was cooled at room temperature, filtered and washed with distilled water and finally dried at 37 °C for 3 h.

Table 2 Comparison of *d*-spacings of the synthesized samples with the standard pattern of Sb_2S_3.

Miller indices	*d*-Spacing (Å)					
	ICSD ref. code No. 03-065-2434	(a) 105 °C/4 h	(b) 150 °C/4 h	(c) 150 °C/6 h	(d) 150 °C/12 h	(e) 200 °C/12 h
201	5.0471	4.5454	4.5281	4.5317	4.5137	
111	3.4545	3.4798	3.4710	3.4655	3.4597	3.4778
211	3.0483	3.1060	3.0996	3.1008	3.1139	3.1323
104	2.7228	2.7329	2.7268		2.7198	
013	2.6774	2.6982	2.6953	2.6923		
113	2.6053	2.6351	2.6341	2.6355	2.6240	
312	2.4236	2.4552	2.4526	2.4515	2.4486	
410	2.2746	2.2656	2.2602	2.2614	2.2566	
105	2.2014	2.2047	2.1993	2.2020	2.1965	
412	2.1079	2.1058	2.1041	2.1093	2.1004	
205	2.0859	2.0577	2.0552	2.0396	2.0368	2.0485
413	1.9406	1.9690	1.9677	1.9665	1.9648	
305	1.9281	1.9311	1.9288	1.9286	1.9252	1.9266
215	1.8323	1.8341	1.8319	1.8317	1.8288	
221	1.7921	1.8053	1.8030	1.8027	1.7994	1.8014
611	1.6718	1.6782	1.6774	1.6774	1.6752	1.6740
612	1.6187	1.6261	1.6265	1.6251	1.6264	
124	1.5675	1.5693	1.5695	1.5692	1.5667	1.5698
224	1.5241	1.5248	1.5227	1.5216	1.5214	1.5215
703	1.4824	1.4883				
515	1.4708	1.4703		1.4699	1.4682	
522	1.4148	1.4171	1.4164	1.4169	1.4152	
008	1.4027	1.4015		1.4016	1.4000	1.3972
620	1.3436	1.3476	1.3451	1.3471		

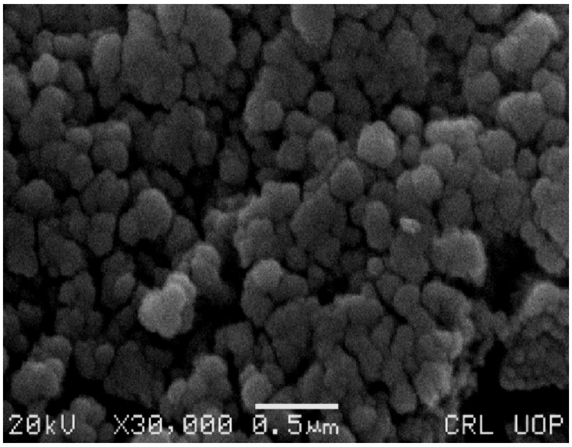

Figure 2 Scanning electron micrograph of the hydrothermally synthesized Sb_2S_3 powder in an autoclave maintained at a temperature of 105 °C for 4 h.

2.2. Characterization of the materials

Phase purity and crystallinity of the prepared powders were studied by powder X-ray diffractometer (PANalytical 3040/60 X'Pert PRO) with Cu Kα radiation source. Diffraction peaks were indexed according to the standard pattern of orthorhombic stibnite powder (ICSD ref. code No. 03-065-2434, a = 11.302 Å, b = 11.222, c = 3.834: V_{cell} = 4.64 Å^3). N_2 adsorption isotherms were used to determine the Brunauer–Emmett–Teller (BET) specific surface area using method employing Quantachrome NovaWin 2. Particle size and surface morphology were studied using scanning electron microscope (JEOL, JSM5910). Thermal analysis was performed on Perkin Elmer (TGA/DTA, Diamond Series) thermal analyser at heating rate of 5° per minute. The FTIR spectra were recorded in the mid-IR region i.e. 400–4000 cm^{-1} using an Excalibur Series Bio-Rad (FTS 3000MX) spectrometer.

2.3. Photocatalytic studies

Methyl orange (MO) was used as a test chemical compound for the photocatalytic studies. 100 mg/L of stock solution was prepared and necessary dilutions were carried out in 50 ml of distilled water in order to prepare 1, 5, 19, 25 and 50 mg/L solutions to study the effect of concentration of MO solution. 0.1 g of catalyst was used in 50 ml of 5 mg/L solution for the study of the effect of pH of solution. Different pH (pH = 4, 7 and 10) were maintained using buffer tablets, the pH of MO solution being 8.5. Catalyst dosage studies were carried out by using 0.1, 0.2, 0.4 and 0.6 g of catalyst in 5 mg/L of solution of MO at room temperature which was maintained at pH 4. Effect of reaction time was studied by taking 50 ml of 5 mg/L MO solution maintained at pH 4 for the time intervals of 1–4 h. Effect of temperature was studied on 50 ml of 5 mg/L MO solution at pH of 4 and temperature was maintained at 35, 70 and 100 °C for 3 h. For the above mentioned studies, the reaction flask was well stirred in the dark for 1 h to maintain adsorption–desorption equilibrium. The absorption spectrum was taken after 1 h dark reaction. The UV response of the catalyst was studied after illuminating the sample with the UV lamp (3UV-38, 4 W) for 1 h. Visible light reactions were carried out in direct sunlight suing concentrating mirrors. The degradation behavior of methyl orange was studied at the λ_{max} of the methyl orange at 470 nm. Aliquots were removed after desired times and the absorption spectra were recorded using T80 UV/vis spectrophotometer. Initial and final absorbance was measured to calculate the concentrations of MO solution and degradation efficiency of the catalyst by using the following equation:

$$\Phi = \frac{C_o - C_t}{C_o} \times 100\% \qquad (1)$$

where C_o is the initial concentration, and C_t is the concentration after time t.

3. Results and discussion

3.1. Characterization of the synthesized material

Phase purity of the synthesized powders under varying temperature and times of reactions in autoclave were studied by X-ray diffraction (XRD) analysis on well ground powders. The standard pattern of stibnite, Sb_2S_3 (ICSD ref. code No. 03-065-2434, a = 11.302 Å, b = 11.222, c = 3.834: V_{cell} = 4.64 Å^3) was taken as a reference pattern. The XRD patterns of the samples

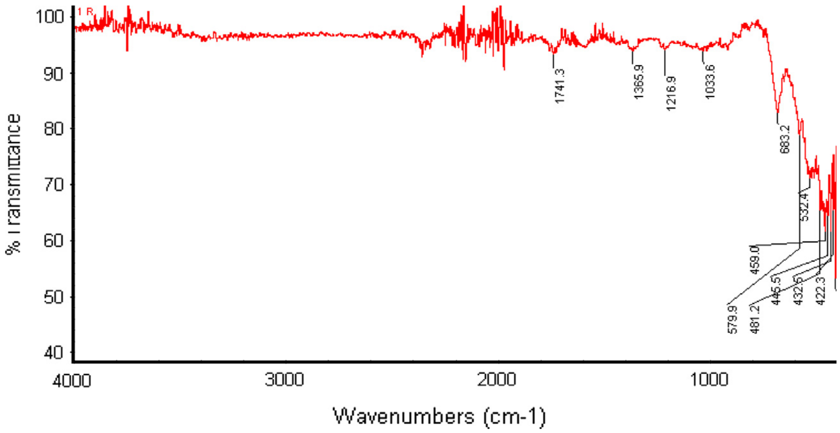

Figure 3 Fourier transform infrared spectroscopy of the hydrothermally synthesized Sb_2S_3 powder in an autoclave maintained at a temperature of 105 °C for 4 h.

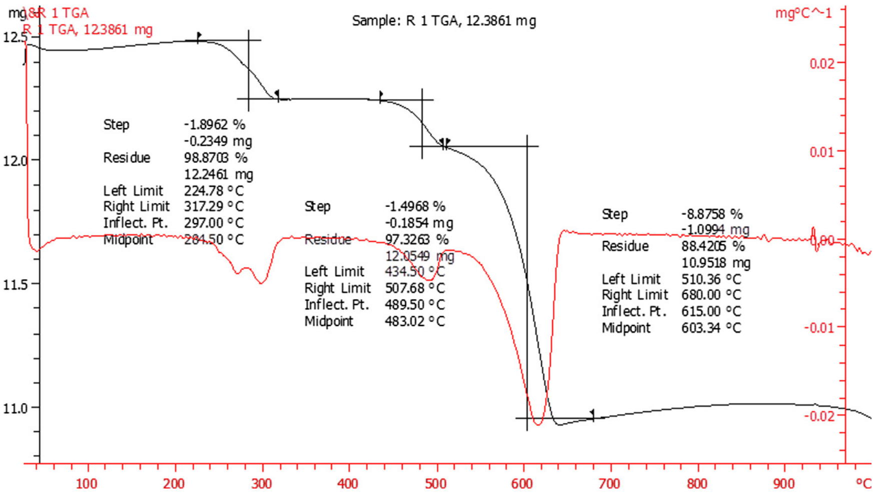

Figure 4 Thermogravimetric analysis of hydrothermally synthesized Sb_2S_3 powder in an autoclave maintained at a temperature of 105 °C for 4 h.

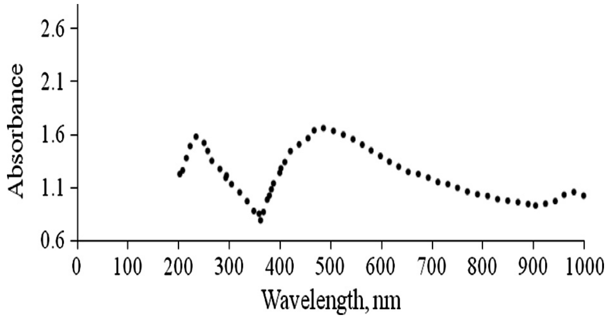

Figure 5 Absorption spectrum of the antimony stibnite powder synthesized at an autoclave temperature of 105 °C for 4 h. Inset: Band gap of the synthesized powder.

synthesized under various conditions are given in Fig. 1. Lattice constants "a, b and c", unit cell volume "V_{cell}", Scherrer crystallite size "D" and X-ray density "$\rho_{\text{X-ray}}$" were calculated using the following relations (Maghraoui-Meherzi et al., 2010):

$$\frac{1}{d^2} = \frac{h^2}{a^2} + \frac{k^2}{b^2} + \frac{l^2}{c^2} \tag{2}$$

$$V_{cell} = abc \tag{3}$$

$$D = \frac{k\lambda}{\beta \cos \theta_B} \tag{4}$$

$$\rho_{\text{X-ray}} = \frac{ZM}{V_{cell} N_A} \tag{5}$$

where d is value of d-spacing, $h\,k\,l$ are corresponding miller indices to each line in the pattern, β is the full width at half maximum of each peak, λ is the X-ray wavelength and is equal to 1.542 Å, θ is the Bragg's angle and k is the constant which is equal to 0.94, Z is the number of molecules per formula unit and is equal to 4 for the orthorhombic crystal structure, M is the molar mass, V_{cell} is the unit cell volume and N_A is Avogadro's number.

The patterns match well with the standard pattern of stibnite indicating the single phase Sb_2S_3 powders synthesized in all the experimental conditions used for the synthesis as shown in Fig. 1. The calculated values of the lattice constants are given in Table 1 along with the corresponding values for the standard pattern. The values of lattice constants a and c are found to be greater than those of the standard pattern while

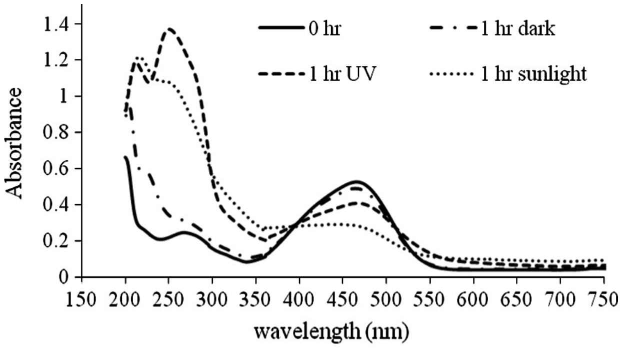

Figure 6 Degradation of 5 ppm solution of methyl orange under dark, UV and sunlight for 1 h.

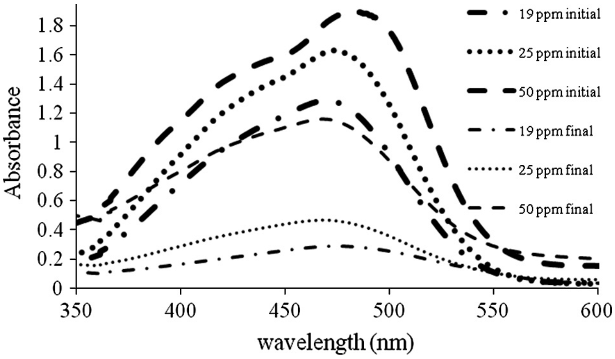

Figure 7 Degradation of 1–50 ppm solution of methyl orange using 0.1 g of catalyst in sunlight for 4 h at a pH of 4 at room temperatures.

those of *b* are lower compared to the standard pattern. The same applies to the increase in cell volumes which is more predominant in the sample synthesized at temperature of 200 °C for 12 h. The X-ray density is found to be lower than the value for the standard sample due to the increase in the cell volume according to Eq. (5). The values of Scherrer crystallite size range from 10 to 50 nm which increases with the increase in the autoclave temperature. The reason for the shift in lattice parameters and corresponding expansion in the lattice may be attributed to the strain in the lattice due to the temperature effects (Deshpande et al., 2005) and increase in grain size. The hydrostatic pressure on grain boundaries is lowered with the increase in grain size which results in lattice expansion (Rane et al., 2013). The comparison of the *d*-spacing of the most intense peaks in the patterns with the standard pattern is given in Table 2. The values match well with the standard pattern. The *d*-spacing values for the planes (2 1 1), (0 1 3), (1 1 3), (4 1 3) and (2 2 1) are slightly shifted to higher values. As no extra peaks are observed in the patterns so reason of shift due to the presence of impurity phase is nullified. Hence, the reason for shift in *d*-spacing may be due to the expansion of lattice as mentioned above. From the view point of temperature and time efficiency, the material synthesized at 105 °C for 4 h was selected for future use and further characterization.

The surface area of the material determined by the N_2 adsorption was found to be 64 m^2/g. The high surface area Sb_2S_3 powder was successfully synthesized in the present study as opposed to other reports (Li et al., 2008; Sun et al., 2008; Han et al., 2010). The pore volume and the pore diameter were 0.16 cc/g and 79 Å respectively. Based on the pore diameter the material was characterized as mesoporous material. The surface morphology as seen under electron micrograph is shown in Fig. 2. The material is porous and smaller particles joined together to form large agglomerates. Almost a homogeneous particle size distribution is seen in the micrographs. The FTIR spectrum of the synthesized material at room temperature is given in Fig. 3. Peaks below 700 cm^{-1} can be assigned to the S—S vibrations or to the S—Sb—S stretching vibrations (Pilapong et al., 2010). C═O and C—N peaks from unreacted urea are seen at ~1700 and 1000–1200 cm^{-1}. The sample synthesized at 105 °C for 4 h was subjected to thermal analysis for the study of thermal stability and TGA pattern of the synthesized material is shown in Fig. 4. Thermal stability of the sample is evident at the studied temperature range of 25–1000 °C with only 12% weight loss in three steps attributed to the loss due to removal of adsorbed water and unreacted reactants.

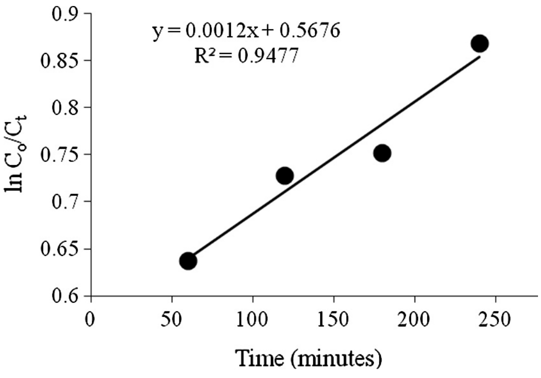

Figure 8 Pseudo first order kinetics followed by the degradation of MO in the presence of photocatalyst.

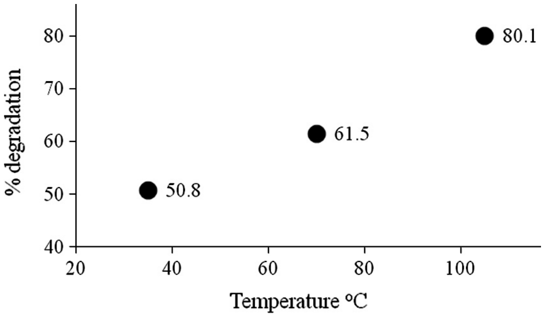

Figure 9 Degradation of 5 ppm solution of methyl orange under different reaction temperatures.

UV/vis absorption spectrum of the synthesized Sb_2S_3 material taken in the form of dispersion was studied in the range of 200–800 nm as shown in Fig. 5. The absorption spectrum showed three regions of absorption, one at ~250–300 nm, a broad absorption peak in the visible region at 350–550 nm and a small absorption peak is observed at 950–1000 nm. The π–π^* transitions and the surface plasmons are found to be responsible for the absorbance in the mentioned regions of electromagnetic spectrum (Subramanian et al., 2010). The indirect and direct band gaps of Sb_2S_3 powders are 1.54 and 1.72 eV (Pilapong et al., 2010; Subramanian et al., 2010) respectively which correspond to energies of the absorbed light in the visible region and higher energy regions of electromagnetic spectrum as shown in Fig. 5.

3.2. Photocatalytic studies

The photocatalytic studies were carried out on the Sb_2S_3 powder synthesized at 105 °C for 4 h in autoclave. For the estimation of the activity of the synthesized material as a photocatalyst, the reaction flask containing 50 ml of 5 mg/L solution of MO and catalyst dosage of 0.1 g at room temperature was maintained for 1 h each in dark (to maintain the absorption–desorption equilibrium), UV light and sunlight. The corresponding UV/vis absorption spectra after each reaction step are shown in Fig. 6. The percent degradation under three conditions was calculated to be 7.4%, 22% and 47% respectively. The high surface area (62 m^2/g) of the synthesized powder could be responsible for the 7.4% removal by the process of adsorption in the dark. Other reports (Li et al., 2008; Sun et al., 2008) achieved ~72% degradation under illumination by Xe lamp and contributions to degradation by adsorption, UV and visible light were also not segregated. After the preliminary test studies, effects of following factors on the visible light degradation efficiency of the synthesized Sb_2S_3 powder have been studied: (a) concentration of the methyl orange solutions, (b) pH, (c) catalyst dosage, (d) time and (e) temperature.

3.2.1. Effect of concentration of the solutions

Fig. 7 shows the degradation efficiency of 0.1 g Sb_2S_3 photocatalyst for 50 ml solution of different concentrations of methyl orange, i.e. 1, 5, 19, 25 and 50 mg/L at room temperature. Two lower concentrations are skipped for clarity of the

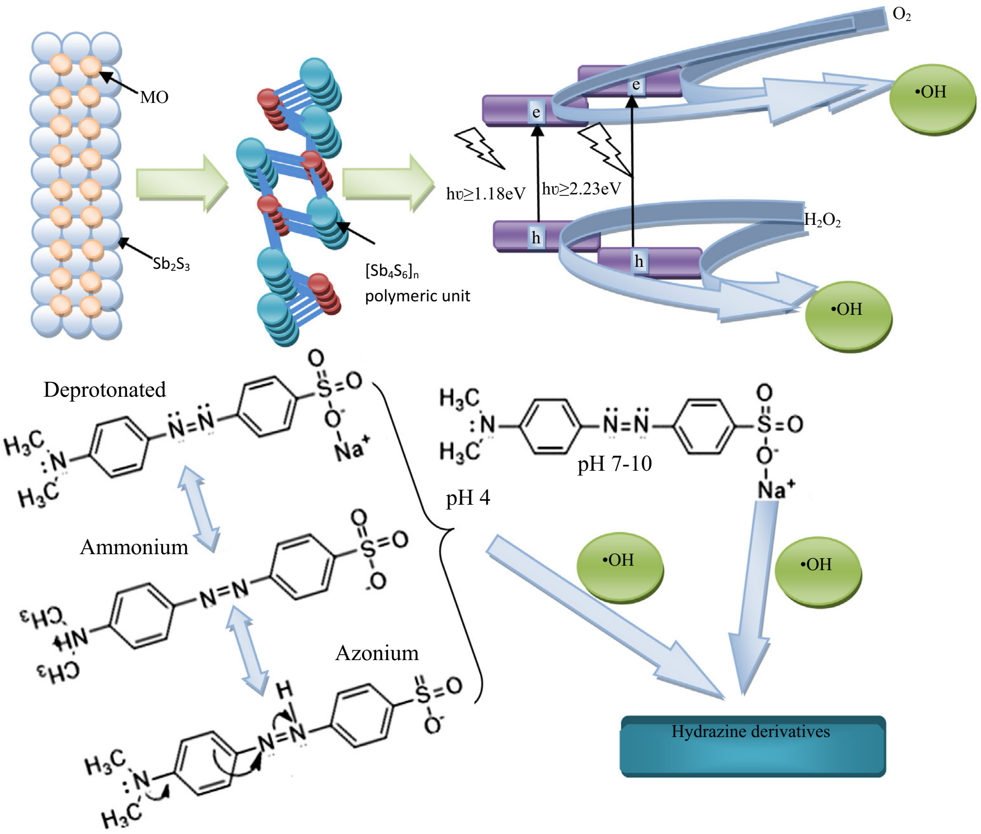

Figure 10 Reaction mechanism for the degradation of MO using Sb_2S_3 powder.

figure. The % degradation of the 1, 5, 19, 25 and 50 mg/L solutions calculated at $\lambda_{\max}$ of MO were 90%, 81%, 77%, 74% and 36% respectively. The increase in dye concentration results in the lower degradation rates. The degradation at the surface of the catalyst is dependent upon (a) generation of $^{\bullet}$OH radicals by the absorption of sunlight by the catalyst, and (b) reaction of $^{\bullet}$OH and the dye. At low dye concentrations, the sunlight is absorbed by the catalyst and the generated $^{\bullet}$OH radicals react with the dye and higher degradation rates are observed. At high dye concentrations, most part of the surface of the catalyst is covered by the dye itself so light is not effectively absorbed by the catalyst. Similarly, the dye itself can absorb sunlight thus reducing the $^{\bullet}$OH generation; hence, lower degradation rates are observed at high dye concentrations (Konstantinou and Albanis, 2004).

3.2.2. *Effect of catalyst dosage*

5 mg/L solution of dye was shaken with different amounts of catalyst ranging from 0.1 to 0.6 g at room temperature. The degradation efficiency calculated for the 0.1, 0.2, 0.4 and 0.6 g of the catalyst dosage was 25%, 57%, 74% and 76% respectively. The degradation rate increases with the increase in the catalyst dosage and then becomes almost constant. The active sites on the catalyst are dependent upon the amount of catalyst. But too much catalyst loading can result in the agglomeration of catalyst resulting in the unavailability of the surface for photon harvesting. The greater catalyst loading may also result in the opacity of the whole reaction flask thereby reducing the degradation efficiency (Guettaï and Ait Amar, 2005).

3.2.3. *Effect of pH*

0.1 g of catalyst was added to 25 ml of 5 mg/L concentration of the dye solution and maintained at pH values of 4, 7, 8.6 and 10 at room temperature. The percent degradation was found to be 81%, 51%, 47% and 40% for the solutions kept at pH 4, 7, 8.6 and 10, respectively. The results indicate the suitability of the lower pH for the degradation. The study of the effect of pH on the photodegradation is a complicated field as pH changes surface characteristic of the catalyst as well as the charge on the dye molecule itself. Methyl orange is an azo dye with a negatively charged sulfonic group so it is an anion. Depending on the pH of solution, it exists either as a protonated form or as a deprotonated form at low and high pH respectively. The protonated form and the negatively charged surface of the catalyst show a positive interaction and hence, better degradation is observed at lower pH (Pires et al., 2012b).

3.2.4. *Kinetic and thermodynamic studies*

The pseudo-first order model has been applied to the degradation reactions of 5 ppm solution of methyl orange kept at room temperature at a pH of 4. The time of reaction was varied from 1 to 4 h in the sunlight. The pseudo-first order kinetics is based on the assumption that the initial degradation reaction step is the attack of OH$^{\bullet}$ radical on the dye molecule, and the generation of OH$^{\bullet}$ radicals remains constant and after the passage of time the degradation by-products also compete with the reaction of OH$^{\bullet}$ and the dye (He et al., 2011).

The rate equation for the pseudo-first order kinetics model is given in Eq. (6) as follows:

$$\ln C_o/C_t = k_{p-1}t \qquad (6)$$

where C_o is the initial dye concentration, C_t is the dye concentration at time t and k_{p-1} is the pseudo-first order rate constant.

The plot of $\ln C_o/C_t$ against t gives a straight line as shown in Fig. 8. The slope is equal to pseudo first order rate constant, the value being 0.0012 min^{-1}.

Different reaction setups of 5 ppm solution of MO utilizing 0.1 g of Sb_2S_3 at pH of 4 were kept in sunlight for period of 3 h and were maintained at temperatures of 35, 70, and 105 °C. The results are plotted in Fig. 9. The increase in degradation is observed with the increase in temperature (Hu et al., 2010).

The summary of the characterization and the degradation reactions would help in proposing the mechanism of reaction. The single phase Sb_2S_3 is confirmed by the XRD and surface area is found to be appreciable for the adsorption of dye. The size of dye can be correlated to the pore diameter obtained from BET. The lower concentrations were degraded well while acidic pH was found to be suitable. The degradation was directly proportional to the amount of catalyst. The intensity of smaller peak below 300 nm increases indicating the formation of some by-products as a result of degradation. The diagrammatic representation of the above mentioned parameters is given in Fig. 10. The crystal structure of Sb_2S_3 is formed of 1-D ribbons of polymerized $[Sb_4S_6]_n$ units. Each ribbon is linked to its four neighbors by weak Sb—S and S—S bonds (Caracas and Gonze, 2005). The absorption of UV and visible wavelengths corresponds to the band gaps that allow the absorption of UV/vis light simultaneously resulting in the generation of electron–hole pairs. The e and holes undergo secondary reactions with the H_2O and O_2 to produce $^{\cdot}OH$ radicals which carry out the degradation reaction on the MO. Now as the reaction was carried out at varying pH conditions, so at pH of 4 both the protonated (azonium and ammonium) and deprotonated forms exist while and at pH 7–10 only deprotonated form exists (Pires et al., 2012a). The $^{\cdot}OH$ radicals react with the dye molecules to produce the hydrazine derivatives as by-products.

4. Conclusion

Photocatalytic studies for the degradation of MO have been carried out on the synthesized antimony sulfide powder. The synthesis was carried out by the hydrothermal method in an autoclave maintained at 105–200 °C for 4–12 h. Effects of time, temperature, concentration, pH and amount of catalyst have been studied. The material was found to be chemically and thermally stable implying longer life times and is cost effective. The mechanism involves the excitation of electrons in the valence band of Sb_2S_3 to the conduction band by the absorption of visible and UV light and the resulting OH radicals participate in the conversion of methyl orange species to hydrazine derivative.

References

Amano, F., Ishinaga, E., Yamakata, A., 2013. Effect of particle size on the photocatalytic activity of WO_3 particles for water oxidation. J. Phys. Chem. C 117, 22584–22590.

Antoniadou, M., Daskalaki, V.M., Balis, N., Kondarides, D.I., Kordulis, Lianos, P., Photocatalysis and photoelectrocatalysis using (CdS–ZnS)/TiO_2 combined photocatalysts. Appl. Catal. B 107, 188–196.

Bessegato, G.G., Cardoso, J.C., Silva, B.F.d., Zanoni, M.V.B., 2013. Enhanced photoabsorption properties of composites of Ti/TiO_2 nanotubes decorated by Sb_2S_3 and improvement of degradation of hair dye. J. Photochem. Photobiol., A 276, 96–103.

Caracas, R., Gonze, X., 2005. First-principles study of the electronic properties of A_2B_3 minerals, with A = Bi, Sb and B = S, Se. Phys. Chem. Miner. 32, 295–300.

Casbeer, E., Sharma, V.K., Li, X.-Z., 2012. Synthesis and photocatalytic activity of ferrites under visible light: a review. Sep. Purif. Technol. 87, 1–14.

Christians, J.A., Kamat, P.V., 2013. Trap and transfer. Two-step hole injection across the Sb_2S_3/CuSCN interface in solid-state solar cells. ACS Nano 7, 7967–7974.

Dantas, T.L.P., José, H.J., Moreira, R., 2003. Fenton and photo-Fenton oxidation of tannery wastewater. Acta Scientiarum Technol. 25, 91–95.

Deshpande, S., Patil, S., Kuchibhatla, S.V., Seal, S., 2005. Size dependency variation in lattice parameter and valency states in nanocrystalline cerium oxide. Appl. Phys. Lett. 87 (133113–133113–133113).

Di Paola, A., García-López, E., Marcì, G., Palmisano, L., 2012. A survey of photocatalytic materials for environmental remediation. J. Hazard. Mater. 211, 3–29.

Guettaï, N., Ait Amar, H., 2005. Photocatalytic oxidation of methyl orange in presence of titanium dioxide in aqueous suspension. Part II: Kinetics study. Desalination 185, 439–448.

Han, Q., Chen, L., Wang, M., Yang, X., Lu, L., Wang, X., 2010. Low-temperature synthesis of uniform Sb_2S_3 nanorods and its visible-light-driven photocatalytic activities. Mater. Sci. Eng., B 166, 118–121.

He, Y., Grieser, F., Ashokkumar, M., 2011. The mechanism of sonophotocatalytic degradation of methyl orange and its products in aqueous solutions. Ultrason. Sonochem. 18, 974–980.

Hu, Q., Liu, B., Zhang, z., Song, M., Zhao, X., 2010. Temperature effect on the photocatalytic degradation of methyl orange under UV–vis light irradiation. J. Wuhan Univ. Technol. – Mater. Sci. Ed. 25, 210–213.

Khataee, A., Fathinia, M., Joo, S., 2013. Simultaneous monitoring of photocatalysis of three pharmaceuticals by immobilized TiO_2 nanoparticles: chemometric assessment, intermediates identification and ecotoxicological evaluation. Spectrochim. Acta Part A Mol. Biomol. Spectrosc. 112, 33–45.

Konstantinou, I.K., Albanis, T.A., 2004. TiO_2-assisted photocatalytic degradation of azo dyes in aqueous solution: kinetic and mechanistic investigations: a review. Appl. Catal. B 49, 1–14.

Korake, P., Dhabbe, R., Kadam, A., Gaikwad, Y., Garadkar, K., 2014. Highly active lanthanum doped ZnO nanorods for photodegradation of metasystox. J. Photochem. Photobiol., B 130, 11–19.

Lee, S.S., Bai, H., Liu, Z., Sun, D.D., 2013. Novel-structured electrospun TiO_2/CuO composite nanofibers for high efficient photocatalytic cogeneration of clean water and energy from dye wastewater. Water Res. 47, 4059–4073.

Li, G., 2011. Intimate Coupled Photocatalysis and Biodegradation on a Novel TiO_2-Coated Biofilm Carrier. Arizona State University.

Li, L., Zhang, M., 2012. Preparation, characterization, and photocatalytic property of Cu_2O–TiO_2 nanocomposites. Int. J. Photoenergy 2012, 1–4.

Li, K.-Q., Huang, F.-Q., Lin, X.-P., 2008. Pristine narrow-bandgap Sb_2S_3 as a high-efficiency visible-light responsive photocatalyst. Scr. Mater. 58, 834–837.

Liang, R., Hu, A., Persic, J., Zhou, Y.N., 2013. Palladium nanoparticles loaded on carbon modified TiO_2 nanobelts for enhanced methanol electrooxidation. Nano-Micro Lett. 5, 202–212.

Litter, M.I., 1999. Heterogeneous photocatalysis: transition metal ions in photocatalytic systems. Appl. Catal. B 23, 89–114.

Liu, Z., Liu, Z., Cui, T., Li, J., Zhang, J., Chen, T., Wang, X., Liang, X., 2014. Photocatalysis of two-dimensional honeycomb-like ZnO nanowalls on zeolite. Chem. Eng. J. 235, 257–263.

Maghraoui-Meherzi, H., Ben Nasr, T., Kamoun, N., Dachraoui, M., 2010. Structural, morphology and optical properties of chemically deposited Sb_2S_3 thin films. Physica B 405, 3101–3105.

Malato, S., Fernández-Ibáñez, P., Maldonado, M., Blanco, J., Gernjak, W., 2009. Decontamination and disinfection of water by solar photocatalysis: recent overview and trends. Catal. Today 147, 1–59.

Morozova, M., Kluson, P., Krysa, J., Dzik, P., Vesely, M., Solcova, O., 2011. Thin TiO_2 films prepared by inkjet printing of the reverse micelles sol–gel composition. Sens. Actuators, B 160, 371–378.

Najam Khan, M., Al-Hinai, M., Al-Hinai, A., Dutta, J., 2014. Visible light photocatalysis of mixed phase zinc stannate/zinc oxide nanostructures precipitated at room temperature in aqueous media. Ceram. Int. 40, 8743–8752.

Nogueira, A.E., Longo, E., Leite, E.R., Camargo, E.R., 2014. Synthesis and photocatalytic properties of bismuth titanate with different structures via oxidant peroxo method (OPM). J. Colloid Interface Sci. 415, 89–94.

Pilapong, C., Thongtem, T., Thongtem, S., 2010. Hydrothermal synthesis of double sheaf-like Sb_2S_3 using copolymer as a crystal splitting agent. J. Alloys Compd. 507, L38–L42.

Pires, M., Ferra, M.I.A., Marques, A.M., 2012a. Ionization of methyl orange in aqueous sodium chloride solutions. J. Chem. Thermodyn. 53, 93–99.

Pires, M.J.R.G.R., Ferra, M.I.A., Marques, A.M.M., 2012b. Ionization of methyl orange in aqueous sodium chloride solutions. J. Chem. Thermodyn. 53, 93–99.

Rane, G.K., Welzel, U., Meka, S.R., Mittemeijer, E.J., 2013. Non-monotonic lattice parameter variation with crystallite size in nanocrystalline solids. Acta Mater. 61, 4524–4533.

Repo, E., Rengaraj, S., Pulkka, S., Castangnoli, E., Suihkonen, S., Sopanen, M., Sillanpää, M., 2013. Photocatalytic degradation of dyes by CdS microspheres under near UV and blue LED radiation. Sep. Purif. Technol. 120, 206–214.

Saranya, M., Santhosh, C., Ramachandran, R., Kollu, P., Saravanan, P., Vinoba, M., Jeong, S.K., Grace, A.N., 2014. Hydrothermal growth of CuS nanostructures and its photocatalytic properties. Powder Technol. 252, 25–32.

Sohrabnezhad, S., Pourahmad, A., Radaee, E., 2009. Photocatalytic degradation of basic blue 9 by CoS nanoparticles supported on AlMCM-41 material as a catalyst. J. Hazard. Mater. 170, 184–190.

Subramanian, S., Balaji, M., Chithra Lekha, P., Asokan, K., Kanjilal, D., Sulania, I., Prakash, J., Pathinettam Padiyan, D., 2010. High-energy ion induced physical and surface modifications in antimony sulphide thin films. Curr. Appl. Phys. 10, 1112–1116.

Sun, M., Li, D., Li, W., Chen, Y., Chen, Z., He, Y., Fu, X., 2008. New photocatalyst, Sb_2S_3, for degradation of methyl orange under visible-light irradiation. J. Phys. Chem. C 112, 18076–18081.

Vidhu, V., Philip, D., 2014. Catalytic degradation of organic dyes using biosynthesized silver nanoparticles. Micron 56, 54–62.

Wang, Y., Wang, F., Jin, F., Jing, Z., 2013. Effects of metals and Ni_3S_2 on reactions of sulfur species (HS^-, S, and $S_2O_{32}^{-}$) under alkaline hydrothermal conditions. Ind. Eng. Chem. Res. 52, 5616–5625.

Xiao, Y., Xu, S., Li, Z., An, X., Zhou, L., Zhang, Y., Shiang, F.Q., 2010. Progress of applied research on TiO_2 photocatalysis–membrane separation coupling technology in water and wastewater treatments. Chin. Sci. Bull. 55, 1345–1353.

Xu, Z., Liang, J., Zhou, L., 2013. Photo-Fenton-like degradation of azo dye methyl orange using synthetic ammonium and hydronium jarosite. J. Alloys Compd. 546, 112–118.

Zhu, G., Liu, P., Miao, H., Zhu, J., Bian, X., Liu, Y., Chen, B., Wang, X., 2008. Large-scale synthesis of ultralong Sb_2S_3 sub-microwires via a hydrothermal process. Mater. Res. Bull. 43, 2636–2642.